Factors controlling ionospheric outflows as observed at intermediate altitudes

R. J. Strangeway,[1] R. E. Ergun,[2] Y.-J. Su,[2] C. W. Carlson,[3] and R. C. Elphic[4]

Received 5 October 2004; revised 6 December 2004; accepted 23 December 2004; published 29 March 2005.

[1] Data acquired by the Fast Auroral Snapshot (FAST) Small Explorer during the 24–25 September 1998 geomagnetic storm have been used to determine the controlling parameters for ionospheric outflows. The data were restricted to dayside magnetic local times. Two primary sources of ion outflows are considered: ion heating through dissipation of downward Poynting flux and electron heating through soft electron precipitation. Ion outflows are shown to be correlated with both, although ion outflows have a higher correlation with soft electrons, measured by the density of precipitating electrons. At 4000 km altitude it is found that $f_i = 1.022 \times 10^{9\pm0.341}\, n_{ep}^{2.200\pm0.489}$, where f_i is the ion flux in $cm^{-2}\ s^{-1}$ and n_{ep} is precipitating electron density, with a correlation coefficient $r = 0.855$, based on log-log regression. This scaling law can be mapped to other altitudes by scaling the flux and density with the magnetic field magnitude. The ion flux is also correlated with the Poynting flux, $f_i = 2.142 \times 10^{7\pm0.242}\, S^{1.265\pm0.445}$, where S is the Poynting flux at 4000 km altitude in $mW\ m^{-2}$ and $r = 0.721$. Either of these two scaling laws can be used specify ion outflow fluxes, since there is a strong intercorrelation between the various parameters. In particular the present study cannot completely eliminate either of the two candidate processes (ion versus electron heating in the ionosphere, corresponding to Poynting flux versus soft electron precipitation). Soft electron precipitation does have a higher correlation coefficient, however, and if possible the precipitating electron density scaling law should be used. Since Poynting flux may be more easily specified in global simulations, for example, this scaling law is a useful alternate. For the interval under study the ion outflows were dominated by oxygen ions, predominantly in the form of ion conics, with a characteristic energy of order 10–30 eV.

Citation: Strangeway, R. J., R. E. Ergun, Y.-J. Su, C. W. Carlson, and R. C. Elphic (2005), Factors controlling ionospheric outflows as observed at intermediate altitudes, *J. Geophys. Res.*, *110*, A03221, doi:10.1029/2004JA010829.

1. Introduction

[2] There has been a long-running debate within the magnetospheric physics community as to the relative importance of the solar wind and ionosphere as sources of plasma for the magnetosphere. To some extent the debate depends on what aspect of magnetospheric physics is being addressed. When considering the ion ring current, for example, the solar wind is often taken to be the primary source of plasma, although observations by the SCATHA spacecraft have indicated the presence of 30 keV oxygen ions that are injected at geosynchronous altitudes in close association with substorm onset [*Strangeway and Johnson*, 1983]. At lower energies, ionospheric outflows may be important as they add mass to flux tubes. This will decrease the Alfvén speed on the flux tubes, slowing the transmission speed of signals through the magnetosphere, and therefore affecting the response of the magnetosphere to changes in external drivers.

[3] At times the mass outflows can be remarkably large. During the 24 and 25 September 1998 geomagnetic storm, ionospheric outflows as high as $7 \times 10^9\ cm^{-2}\ s^{-1}$ were observed at 4000 km altitudes in the dayside cusp region [*Strangeway et al.*, 2000]. Taking an area at this altitude of 2000 km by 2000 km (10° by 10° at the ionosphere), this corresponded to an oxygen mass outflow of $\sim$7 kg s^{-1} or 3×10^{26} oxygen ions/s. This is as large as the total oxygen outflows, integrated over both hemispheres, reported by *Yau and André* [1997] for $K_p = 6$ and solar maximum conditions (their Figure 14).

[4] This mass outflow was associated with a large coronal mass ejection (CME) that resulted in significant fluxes of oxygen in the high-latitude cusp, as observed by the Polar spacecraft [*Moore et al.*, 1999]. The ion outflows were clearly driven by processes associated with the enhanced solar wind dynamic pressure and interplanetary magnetic field (IMF) that followed the CME-driven interplanetary shock. On the basis of the work of *Pollock et al.* [1988],

[1]Institute for Geophysics and Planetary Physics, University of California, Los Angeles, California, USA.
[2]Laboratory for Atmospheric and Space Physics, University of Colorado, Boulder, Colorado, USA.
[3]Space Sciences Laboratory, University of California, Berkeley, California, USA.
[4]Los Alamos National Laboratory, Los Alamos, New Mexico, USA.

0148-0227/05/2004JA010829$09.00

Moore et al. [1999] argued that fluctuations in solar wind dynamic pressure, rather than the enhanced dynamic pressure itself, drove the outflows. Although not discussed explicitly by Moore at al., presumably the pressure fluctuations would in turn drive Alfvén waves from the magnetopause into the high-latitude ionosphere. These waves could then heat ions in the topside ionosphere, thereby inducing outflows.

[5] This model was questioned by *Strangeway et al.* [2000] on the basis of observations by the Fast Auroral Snapshot (FAST) Explorer [*Carlson et al.*, 1998]. The FAST orbit was such that during the outflow interval the spacecraft passed through the dayside cusp in the noon-midnight meridian at 4000 km altitude. FAST was therefore able to observe directly the escaping ions that were subsequently detected by the Polar spacecraft. *Strangeway et al.* [2000] noted that following the passage of the interplanetary shock a strong cusp region field aligned current system was set up, driven by reconnection with the IMF B_y, which was ~+30 nT. The observed current system appeared to be consistent with that presented by *Cowley* [1981], where the cusp-region currents are best represented as an overlap of dayside region-1 currents, rather than a separate current system (see Figure 4c of *Strangeway et al.* [2000]). The shearing of dayside region-1 currents to form cusp currents has also been discussed by *Zhou et al.* [2000] and is consistent with the antiparallel merging model of *Crooker* [1979], where the direction of the shear of the current systems is dictated by the direction of the IMF B_y. The strength of the current system depends on the stresses applied to the magnetosphere by reconnection at the magnetopause.

[6] *Strangeway et al.* [2000] noted that the amount of Poynting flux flowing into the ionosphere changed by orders of magnitude before and after the shock transition. On the basis of a limited sample (five passes of FAST through the outflow region), they demonstrated a statistically significant correlation between peak Poynting flux and peak ion outflow fluxes. They further argued that the enhanced Poynting flux would heat ions in the lower ionosphere and that these ions would form a seed population that would be heated at higher altitudes to form escaping ion conics. A multistep process is required since the Joule dissipation may heat ions sufficiently to cause upwelling but not escape. Additional wave heating is required to bring the heavier ions (e.g., oxygen) to high enough energy to overcome gravity. At even higher altitudes these ions may also undergo centrifugal acceleration [*Cladis*, 1986].

[7] In arguing that Poynting flux controlled ion outflow rates, *Strangeway et al.* [2000] noted that by balancing Joule dissipation rates with cooling by collisions with neutrals, a direct relationship can be found between ion temperature and incoming Poynting flux, as shown in (1) (see also *Banks and Kockarts* [1973], equation 22.12, and *Horwitz* [1996], equation 1). In SI units

$$k_b(T_i - T_n) = \frac{m_n v_i^2}{3} \frac{m_n S_F}{3\Sigma_p B_0 B_F}, \qquad (1)$$

where T_i is the ion temperature, T_n is the neutral temperature, m_n is the neutral mass, v_i is the ion velocity with respect to the neutrals, S_F is the Poynting flux at the altitude of FAST, Σ_p is the Pedersen conductivity, B_0 is the ambient magnetic field at the ionosphere, and B_F is the ambient magnetic field at FAST altitude. We have assumed frozen-in ions and made use of $E = \delta B/\mu_0\Sigma_p$.

[8] One problem with this model is that while (1) is independent of collision frequency, we do not expect this equilibrium to apply when the collision frequency is smaller than the time constants of other processes, such as convection. Thus it is generally accepted that the ion heating associated with Joule dissipation is restricted to the E and lower F regions of the ionosphere, implying that the upwelling produced may be relatively weak. An alternative source of ion heating is the precipitation of soft electrons (<500 eV) [*Liu et al.*, 1995; *Horwitz*, 1996]. This was demonstrated clearly by *Ogawa et al.* [2000], who used radar observations to compare in situ ionospheric ion and electron temperatures with field-aligned ion flow velocities. They showed that the ion upwelling was mainly associated with enhanced electron temperatures. Electron heating causes ion upwelling through the ambipolar electric field associated with an enhanced electron temperature. Because the electron heating occurs at higher altitudes, it is often argued that this will result in greater outflows than ion heating at lower altitudes.

[9] *Strangeway et al.* [2000] did not assess the importance of electron precipitation in their earlier work, and it is therefore essential that we revisit the analysis including precipitating electrons as a potential driver of ion outflows. The dayside cusp is an obvious location for soft electron precipitation; indeed this is one of the characteristics of cusp field-lines, where magnetosheath electrons enter the magnetosphere.

[10] Figure 1 presents a flow chart showing the two principal pathways for generating ionospheric outflows. The left-hand side shows the flow of electromagnetic energy, via Poynting flux, while the right-hand side shows the particle energy flow, primarily through soft electron precipitation. As already noted, Poynting flux results in ion frictional heating, which increases the ionospheric scale height, while electron precipitation heats ionospheric electrons. This also increases the scale height through the generation of an ambipolar electric field. It should be further noted that while (1) shows a clear relationship between Poynting flux and ion heating, the role of electron precipitation is more complicated. Electron heating is not just a function of electron energy flux but also depends on the hardness of the spectrum. Higher-energy electrons tend to penetrate too deeply into the ionosphere. This will also become clear in our statistical analysis. Furthermore, while both processes therefore result in ionospheric upwelling, neither process heats the ions sufficiently for them to escape, and so transverse wave heating is invoked to generate ion conics, which then can escape.

[11] The upper portion of Figure 1 shows parameters as measured at FAST altitudes. Each connecting arrow is labeled with a correlation coefficient derived from the statistical analysis presented in this paper. The lower portion of the figure shows processes inferred to occur at lower altitudes. The arrows connecting the various cells are labeled "causal," "possibly causal," and "correlated." The "causal" arrows indicate processes that are known to be causally related, while the "possibly causal" arrows

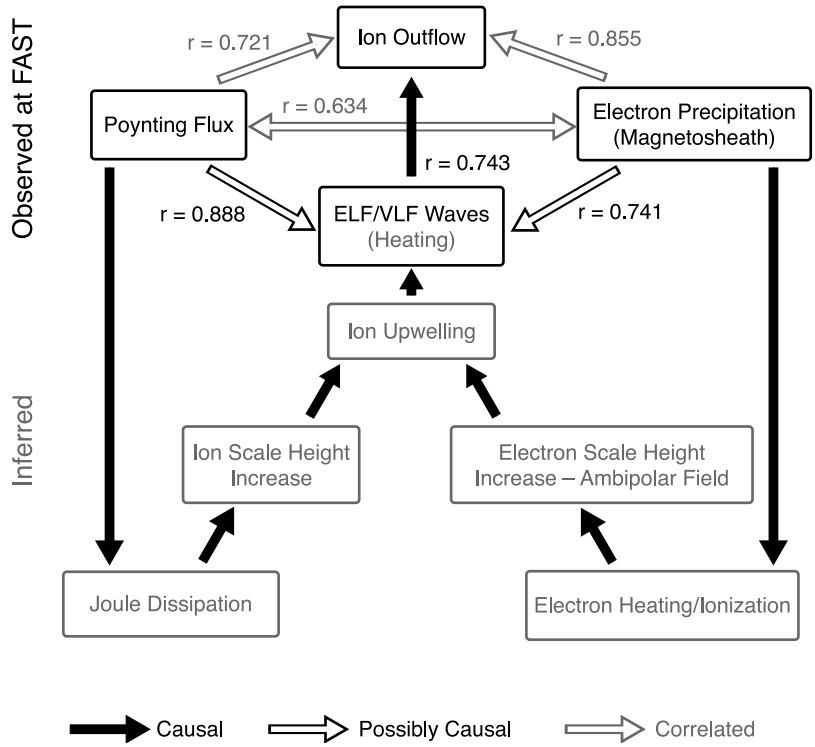

Figure 1. Flow chart showing the relationship between energy inputs to the ionosphere and ion outflows. The upper half of the diagram corresponds to observations at FAST, while the lower half is the inferred pathway whereby Poynting flux or electron precipitation results in ion upwelling and subsequent outflows. The numbers labeling the arrows are correlation coefficients based on log-log regression, derived from the statistical analysis presented in section 3.

indicate processes that could reasonably be causally related. For example, the field aligned currents associated with the large scale Poynting flux could generate ELF waves through current driven instabilities, and by the same token the precipitating electrons could also generate waves. The last type of arrow, indicated by grey, shows processes that are correlated but do not have a direct causal relationship. In particular, both downward Poynting flux and soft electron precipitation tend to occur in the cusp region. Both are related to reconnection at the magnetopause, but the Poynting flux does not cause cusp electron precipitation and vice versa, although even here a caveat is in order. Any process that results in dissipation of the Poynting flux (e.g., parallel electric fields in regions of field-aligned current) will lead to particle energization, thereby transferring energy from the pathway on the left-hand side to the right-hand side.

[12] We explore the statistical relationship between various potential drivers of ion outflows as observed at FAST altitudes for two reasons. The first is to determine which is the best controlling parameter. The second is to provide scaling laws that can be used in computational models that wish to include ionospheric outflows [e.g., *Winglee et al.*, 2002] but with a variable rate dependent on external drivers. These scaling laws should be viewed as complementary to other laws that provide outflow rates as a function of indices such as A_e or K_p [e.g., *Peterson et al.*, 2001, and references therein].

[13] A word of caution is in order with regard to correlative studies such as this. Correlation is not causality, and while strongly indicative of a causal relationship, some other tests may be required to provide definitive proof of causality, especially if the difference between correlation coefficients is small.

[14] The outline of the paper is as follows. The next section presents an example of the FAST data used in this study. While the FAST particle and fields data include measurements as a function of energy and angle for the particles and frequency for the wave fields, these are reduced to integrals as discussed in section 2 and Appendix A in order to perform correlative studies. Section 3 presents the results of the statistical analysis, while section 4 discusses the significance of these results. In particular, we find that the single best controlling factor for determining ion outflow rates is the precipitating electron density, although DC Poynting flux can be used as a proxy in lieu of measurements of precipitating electron fluxes. We also derive scaling laws that could be used to parameterize ion outflows as a function of these two controlling factors, which may be useful in large-scale simulations, for example. The concluding section summarizes our results and also describes future studies that follow on from the work presented here.

2. FAST Data Overview

[15] Figure 2 shows FAST data acquired on orbit 8276, 25 September 1998. These data were discussed by *Strangeway et al.* [2000] in arguing that Joule dissipation associated with the large-scale cusp current system was an important factor in driving outflows. From top to bottom the figure shows electron differential energy flux as a function

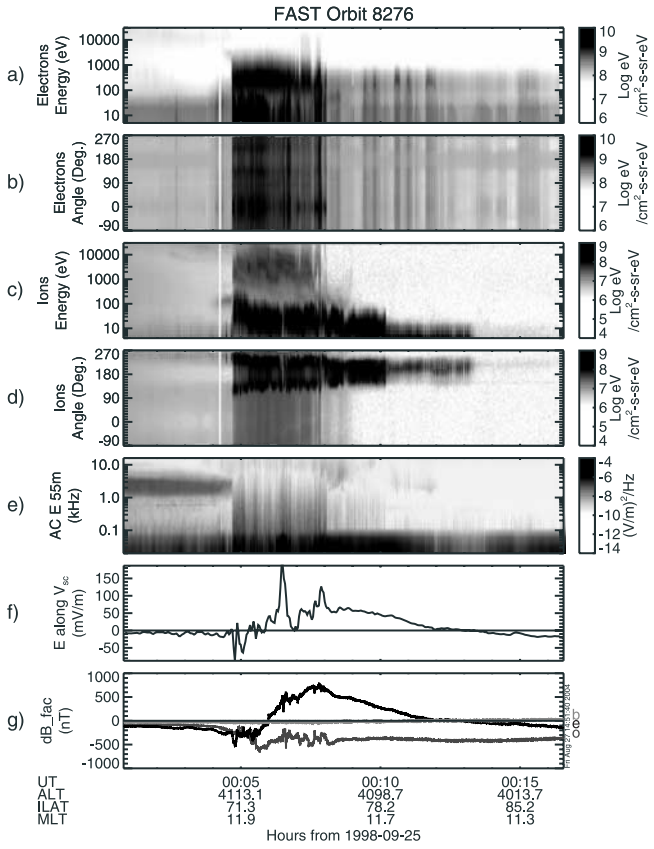

Figure 2. Summary plot of FAST data acquired on orbit 8276. The figure shows electron differential energy flux as a function of (a) energy and (b) pitch angle; ion differential energy flux as a function of (c) energy and (d) pitch angle; (e) ELF wave power, acquired using an onboard Digital Signal Processor (DSP); (f) spin-averaged electric field, measured along the spacecraft velocity vector projected into the spin plane; and (g) the magnetic field deviations from the IGRF model field, in field-aligned coordinates.

of energy (Figure 2a) and pitch angle (Figure 2b), ion differential energy flux as a function of energy (Figure 2c) and pitch angle (Figure 2d), the ELF wave spectra from 30 Hz to 16 kHz (Figure 2e), the electric field as measured in the spin plane (Figure 2f), nominally along the spacecraft velocity vector, and the deviations in the magnetic field cast into field-aligned coordinates (Figure 2g). The field-aligned coordinates are such that the black trace in Figure 2g shows the deviation from the IGRF model field in the direction perpendicular to the magnetic meridian, positive to the east.

[16] The data in Figure 2 were acquired as FAST entered the polar cap on the dayside in the noon-midnight local time sector. Shortly after 0004:30 UT, the spacecraft crossed into the polar cap. Immediately on crossing this boundary, strong fluxes of precipitating magnetosheath electrons were observed, with characteristic energies around 300 eV (Figure 2a). At the same time, magnetosheath ions with energies around 1 keV were observed (Figure 2c), as well as intense ion conics (Figure 2d). In this study most of the ion outflows were associated with ion conics. A large field-aligned current was also seen, with a net eastward deflection of ~1200 nT (Figure 2g). This downward current was observed in a region of strong electron precipitation, but unlike the nightside auroral zone "inverted-V" electrons, the precipitating electrons did not determine the polarity of the current. It is assumed that upflowing low-energy electrons, below the energy threshold of the detector, carry the downward current. The magnetosheath particles are characteristic of the cusp as observed at FAST altitudes. The magnetic field deflection is also characteristic of the throat region, whose orientation is controlled by the IMF B_y [*Cowley*, 1981]. After 0008 UT the spacecraft leaves the region of strong magnetosheath particle precipitation and enters the polar cap proper. Ion outflows and precipitating magnetosheath electrons are still observed, although both are somewhat weaker than in the cusp.

[17] In their earlier analysis, *Strangeway et al.* [2000] correlated the peak Poynting flux with the peak upward ion flux as measured over the interval where outflows are observed. Given the highly variable structure of the outflows, it is not clear that the peak fluxes are representative of the outflows. In this study we will use two different statistical measures. The first is the average, calculated by integrating over the interval for which outflows are observed. The average is a more robust measure than the peak, but by being restricted to the interval over which outflows are observed, we do not test the null hypothesis that an energy input (be it carried by particles or fields) is not associated with outflows. To address this, we also perform a point-by-point correlation analysis. The data used for such a correlation analysis are shown in Figure 3.

[18] The data in Figure 3 are 1-s averages of the various energy inputs and associated ion outflow fluxes. Because the data rates are different for the different experiments on board FAST it is necessary to both average and resample the data. To do this, we first integrate the particle fluxes to obtain energy fluxes and number fluxes for both ions and electrons. These fluxes are then smoothed with a five-point window and interpolated to make a uniformly spaced time series with 1-s resolution. For the electrons the fluxes are restricted to energies above 50 eV to remove photoelectron contamination, while the ions fluxes are restricted to energies below the precipitating magnetosheath and plasma sheet ions, i.e., typically below 100 eV, although this limit is increased if the conic energy exceeds 100 eV, as is the case for the data in Figure 2. See Appendix A for a more detailed discussion on the various limits used in determining ion fluxes.

[19] The ELF wave spectra are integrated over frequency to give net wave electric field amplitude. At this stage we do not distinguish between the various wave modes associated with ion outflows (see *André et al.* [1998] for a complete discussion on the different ELF waves observed at polar latitudes). Furthermore, while ELF is strictly speaking defined as the frequency range from 300 Hz to 3 kHz, we are using ELF as shorthand for the entire spectral bandwidth of the wave instrument, from 30 Hz to 16 kHz. This frequency band includes high-frequency Alfvén waves, ion cyclotron waves for oxygen and hydrogen, and low-frequency whistler mode waves, as well as broadband ELF (BBELF). A statistical analysis of the importance of different wave modes as observed at Freja altitudes (1700 km) is presented by *Hamrin et al.* [2002].

[20] Last, the magnetic and electric fields are smoothed down to 4-s resolution and then interpolated to 1-s data. The

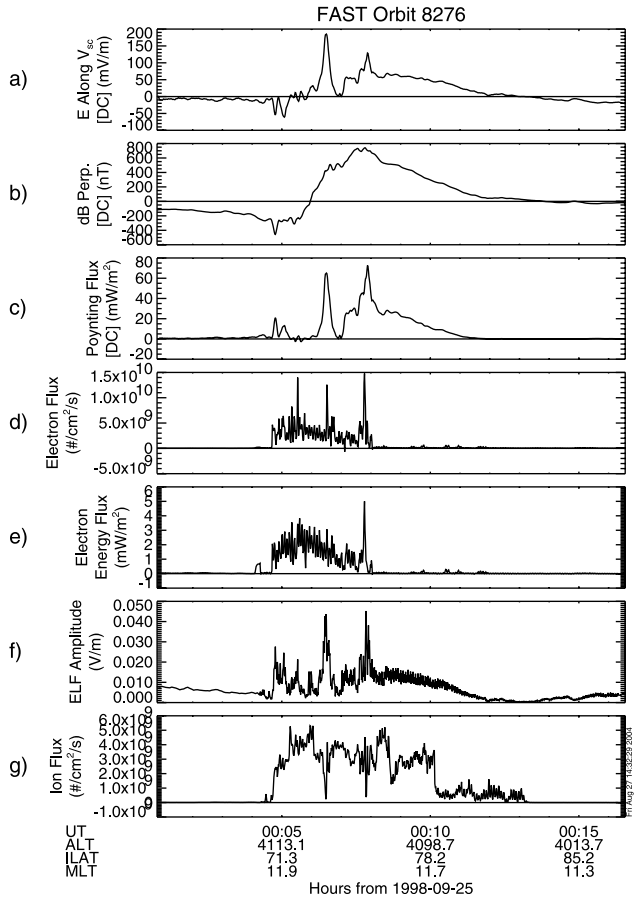

Figure 3. One-second averages of the data used for the statistical survey, corresponding to the interval shown in Figure 2. The figure shows (a) filtered electric field and (b) perpendicular magnetic field data; (c) the associated "DC" Poynting flux, positive downward; (d) electron number and (e) energy flux, both positive downward; (f) ELF amplitude; and (g) ion number flux, positive upward. The methodology used to obtain these averages is described in Appendix A.

choice of 4 s is somewhat arbitrary, but the intention is to remove any high-frequency fluctuations that might be associated with Alfvén waves. The role of Alfvén waves in controlling outflows will be discussed elsewhere. Obviously, variations in the electric and magnetic fields with periods longer than 4 s could correspond to Alfvén waves. At high latitudes in the polar cap, however, we expect the Alfvén speed to be of the order 10^4 km/s or faster. Any Alfvén wave observed at FAST altitudes with variations slower than 4 s will therefore be a standing wave, with the electric field/magnetic field ratio being determined by the ionospheric boundary condition, i.e., $E = \delta B/\mu_0\Sigma_p$, as is also the case for large-scale field-aligned currents. The 4-s filter therefore ensures that the signals are restricted to those that result in frictional Joule dissipation in the lower ionosphere. The Appendix also shows that the 4-s filter does tend to separate the data into Alfvén-like and DC-like signals, where $E/\delta B$ is determined by the Alfvén speed for the former and Σ_p for the latter.

[21] The 1-s data enable the assessment of both positive and negative correlation between outflows and energy inputs. For example, before 0430 UT in Figure 3 no ion outflow is detected, although energy flows into the ionosphere as Poynting flux, albeit at a much lower level than at higher latitudes. This is typically the case at lower latitudes on the dayside, below the polar cap boundary.

3. Statistics

[22] We have analyzed data from 33 orbits, centered on orbit 8276. The orbital coverage in magnetic local time and latitude is shown in Figure 4, with the intervals of ion outflows marked by the thick line segments. Generally, the lower-latitude portion of the region of ion outflows is associated with the cusp, especially near noon. At higher latitudes and local times nearer to dusk the precipitation fluxes are weaker, and the ion outflows are in the polar cap, rather than the cusp. As discussed in the previous section, we use both averages and 1-s resolution data to characterize the outflows. Figures 5–8 show the relationship between the different inputs and the associated ion outflows, using the average data. These figures show the relationship between ion outflow fluxes and Poynting flux (Figure 5), downward electron energy flux (Figure 6), downward electron number flux (Figure 7), and ELF wave amplitude (Figure 8). These parameters were chosen to represent the role of ion heating within the ionosphere (Poynting flux, left side of Figure 1), electron heating in the ionosphere (electron energy and number flux, right side of Figure 1), and ion conic formation (ELF wave amplitude, center path of Figure 1). Because the pathway by which precipitating electrons heat the ionosphere is complicated, at this stage we consider both energy flux and number flux in the correlation analysis. For each figure the data are plotted on a logarithmic scale and the regression

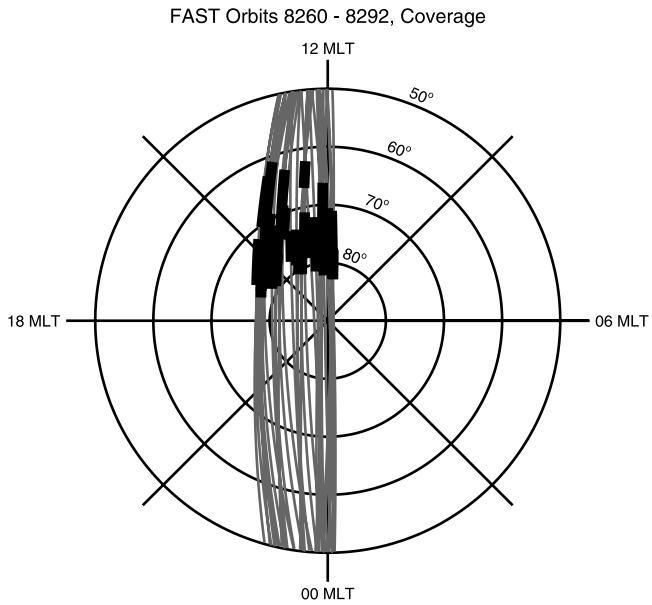

Figure 4. Orbital coverage for the 33 orbits used in the study. The thick black line segments indicate regions in which ion outflows are observed. The coverage is such that most of the outflows are observed in the postnoon local time sector on the dayside. In this paper we only consider data acquired on the dayside (0600 < MLT < 1800).

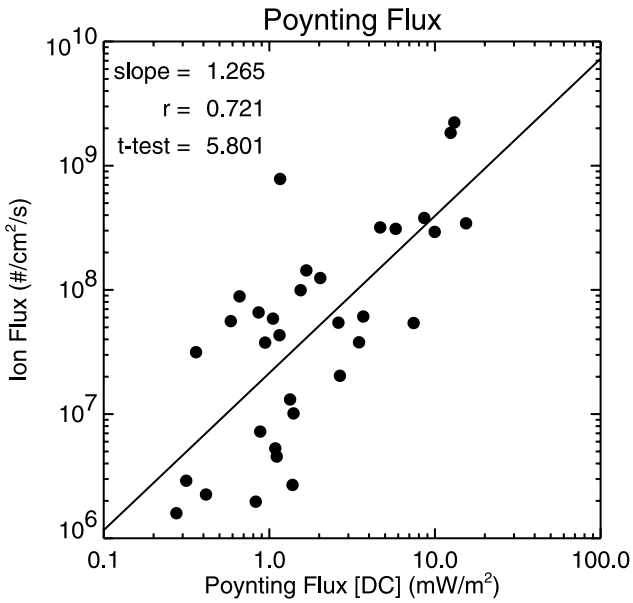

Figure 5. Correlation between average ion fluxes and average DC Poynting flux. The averages only include data during which outflows are observed, as indicated in Figure 4. Each point corresponds to a single orbit average.

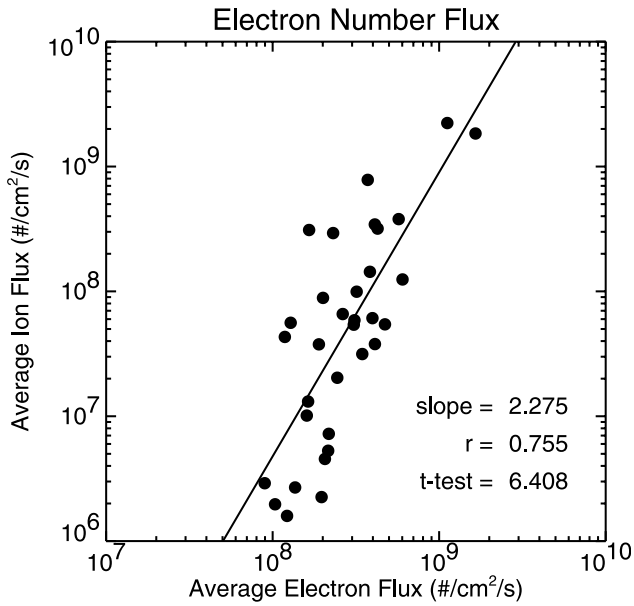

Figure 7. Correlation between orbit averages of ion outflow fluxes and average electron number flux.

analysis uses the $\log_{10}$ of the data. The slope of the regression line therefore indicates the power to which the independent variable is raised in the correlation. For example, from Figure 5, $f_{in} \propto S^{1.265}$, where f_{in} is the average ion number flux in cm^{-2} s^{-1}, and S is the average Poynting flux in mW m^{-2}.

[23] Figures 6 and 7 show that when plotted logarithmically, the ion outflow fluxes are negatively correlated with the electron energy flux but positively correlated with the electron number flux. This is probably a signature that the electron heating within the ionosphere and the associated ionospheric upwelling is favored by soft (<500 eV) electrons. Higher-energy electrons tend to penetrate to lower altitudes, where the heating is less efficient [*Liu et al.*, 1995; *Horwitz*, 1996].

[24] Most of the parameters shown in Figures 5–8 have a statistically significant correlation with the ion outflow fluxes (for 33 data points a correlation is significant at the 95% level if the Student's t statistic is >2.040). Only the electron energy flux has a statistically insignificant correla-

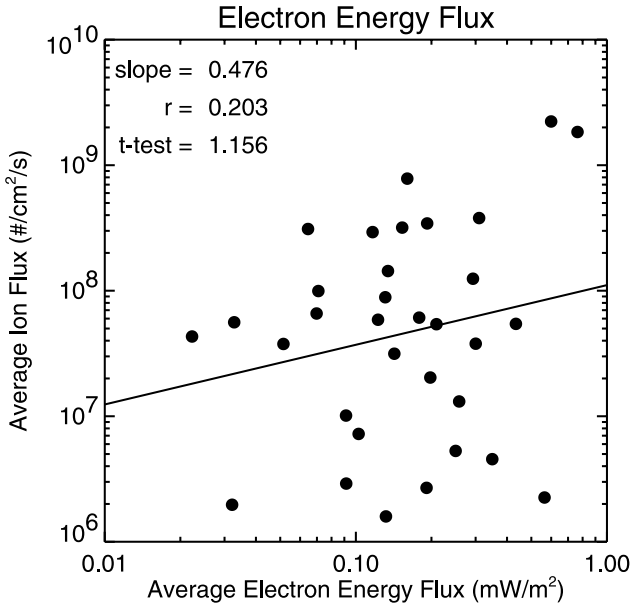

Figure 6. Correlation between orbit averages of ion outflow fluxes and average electron energy flux. The outflows are weakly anticorrelated with electron energy flux.

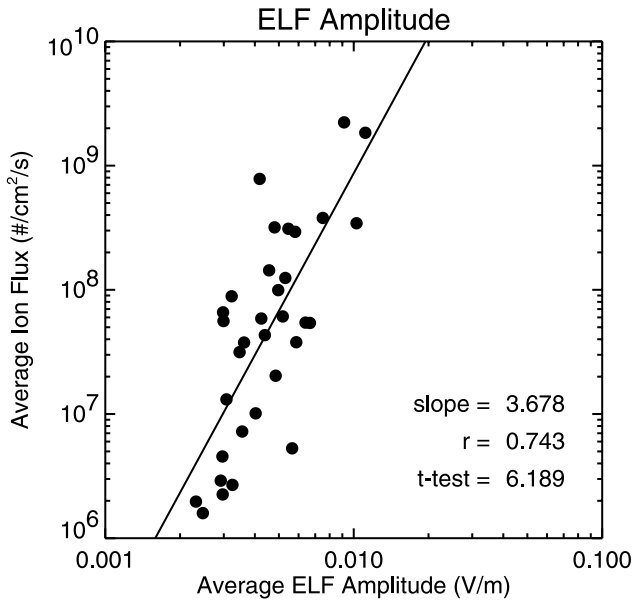

Figure 8. Correlation between orbit averages of ion outflow fluxes and ELF wave amplitudes.

Table 1. Slopes of the $\log_{10}$- $\log_{10}$ Multiple Linear Regression for the Different Controlling Parameters[a]

Poynting Flux	Number Flux	Energy Flux	ELF Amplitude	$F_{1,29}$ Test
0.59	2.60	−1.20	0.07	
Deleted	2.52	−1.22	1.68	3.49
0.44	Deleted	−0.46	3.05	29.46
0.66	1.45	Deleted	0.16	21.21
0.61	2.62	−1.20	Deleted	0.004

[a]The $F_{1,29}$ test statistics is used to determine if the parameter marked as deleted is not significant for the regression. If $F_{1,29} < 4.18$, a parameter can be rejected at the 95% confidence level.

tion. Through multiple linear regression, we can determine which of the individual controlling parameters best determine the ion outflow fluxes. In multiple linear regression all four of the parameters plotted on the abscissa are taken as independent variables, although this assumption may be invalid. Table 1 shows the slopes determined from the multiple linear regression, again using $\log_{10}$ of the data. The first row of the table shows the slopes for all four parameters, with subsequent rows showing the slopes as determined when one of the parameters is deleted from the regression analysis. The last column in the table shows the F-test statistic that compares the variance of the fit to that expected for random coincidence. In this case the test statistic is given by the change in residual variance on removing one parameter divided by the mean residual variance for the four-parameter fit. The latter assumes 29 degrees of freedom. If the test statistic is less than 4.18 (95% confidence level) then the deleted parameter can be considered to be unimportant in terms of the regression analysis. We emphasize that this does not mean that the parameter is also physically unimportant, only that it can be subsumed into one of the other controlling parameters, again emphasizing that the regression analysis assumes statistical independence, which may not be valid.

[25] Table 1 indicates that the electron number and energy flux are sufficient to explain the correlation, which appears to contradict the data shown in Figure 7, where the electron energy flux on its own was not correlated at the 95% level. Both the Poynting flux (Figure 5) and ELF wave amplitude (Figure 8) were statistically more significant when treated independently, yet these two variables can be dropped from the analysis using multiple linear regression. Again this underscores the lack of independence between the various assumed controlling parameters.

[26] We can combine both the number flux and energy flux to give a single parameter that characterizes the precipitating electrons. Noting that the energy flux divided by the number flux gives a characteristic energy, we can define a regression parameter that has the dimensions of number density, which is

$$n_{ep} = 2.134 \times 10^{-14} f_{en}^{3/2} / f_{ee}^{1/2}, \quad (2)$$

where n_{ep} is the "precipitating" electron number density in cm^{-3}, f_{en} is the electron number flux in $cm^{-2}\ s^{-1}$, and f_{ee} is the electron energy flux in mW m^{-2}. We refer to n_{ep} as the precipitating number density since it is determined from the number flux, which is positive for net downward flux. The regression analysis for this parameter gives $f_{in} \propto n_{ep}^{2.200}$, with a correlation coefficient $r = 0.855$. For this correlation, f_{en} and f_{ee} are given by the averages over the outflow intervals.

4. Discussion

[27] Figure 1 was used earlier in this paper to introduce the two pathways for generating ionospheric outflows. As noted earlier, each arrow connecting parameters measured at FAST altitudes is labeled with the corresponding correlation coefficient, again based on log-log regression of averages over the intervals of active outflows for the 33 orbits discussed earlier. Following our earlier discussion, the soft electron precipitation is characterized by the precipitating electron density, n_{ep}.

[28] We have already discussed the meaning of the different types of arrows connecting the cells in Figure 1. We specifically noted that downward Poynting flux and soft electron precipitation are correlated but not causally related. It should be noted, however, that the correlation between Poynting flux and precipitating electrons is the lowest of those shown in Figure 1.

[29] One possible conclusion to be drawn from Figure 1 is that Poynting flux may contribute to ion outflows through more than one pathway. On the basis of the order of the correlation coefficients it may be that the Poynting flux contributes to the generation of ELF waves, possibly through current-driven instabilities, and it is this pathway that relates Poynting flux to ion outflows, rather than the Joule dissipation pathway. However, it must be remembered that correlation does not prove causality and may only indicate hypotheses that require further testing. Furthermore, it should also be noted that the ELF measurements are obtained by integration of the wave power spectral density. The spectra may also include some portion of the large-scale (DC) electric field, as discussed further in Appendix A. At the same time, it appears from the correlation coefficients that waves generated by soft electrons are only a secondary effect, and the primary causal pathway on the right of the figure is more likely to explain the strong correlation between electron precipitation and ion outflows.

[30] On the basis of the correlations presented above we can derive scaling laws that relate the electromagnetic and particle fluxes to ion outflows. In doing so, however, we should also recognize the correlations presented here are based on averages over the regions of ionospheric outflows. The averages do not take into account fine structure in the outflows, some of which is evident in Figure 3, nor do the averages address the null hypothesis where downward Poynting flux or electron precipitation are present without any corresponding outflows. We shall investigate this further based on correlations between the 1-s averages.

[31] Figure 1 indicates that soft electron precipitation may be the dominant controlling factor. Figure 9 compares the regression based on integration over regions of ion outflow with the underlying 1-s data. The 1-s data are acquired over the dayside polar ionosphere. In this study we have restricted the energy range of the ion outflow fluxes based on the observed cusp-region conic. Nightside flows will not have the same energy range restriction and have therefore not been included. The figure takes into account negative fluxes in the scatter plot by plotting both positive and negative

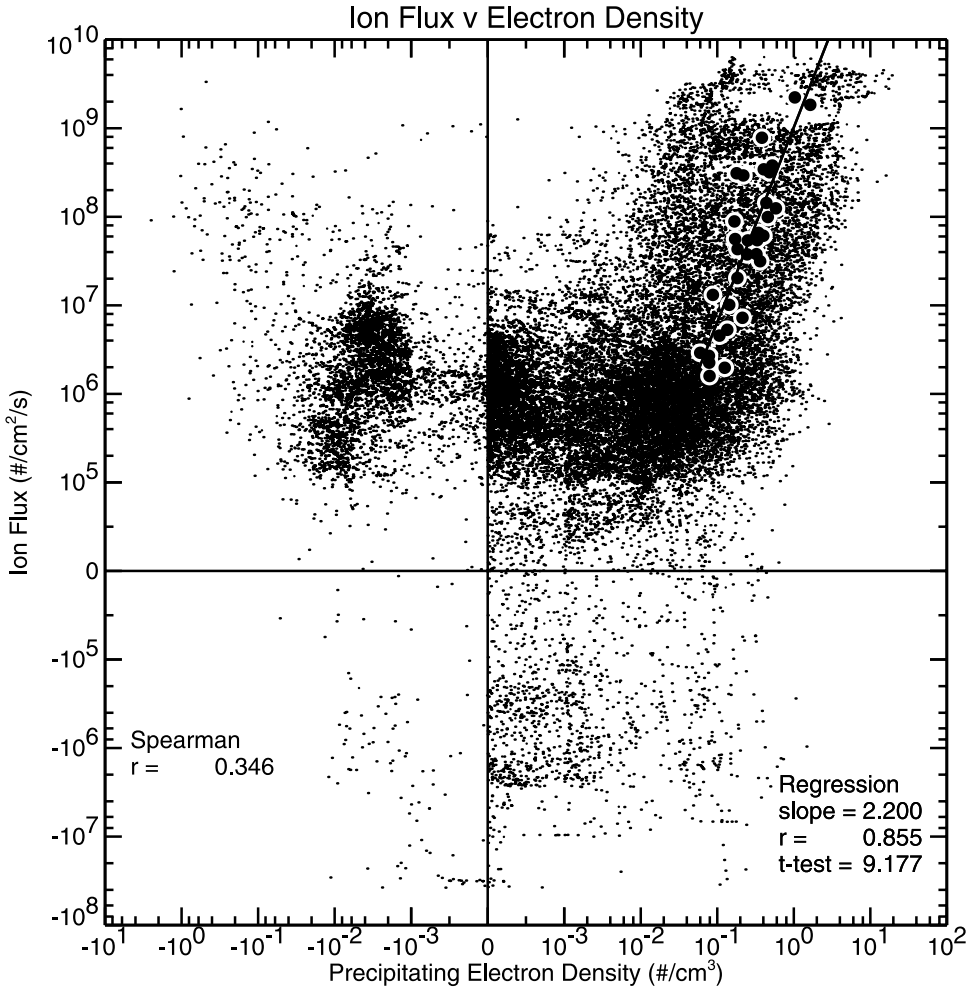

Figure 9. Scatterplot showing relationship between precipitating electron density as defined by (2) and ion flux. In order to show negative fluxes the figure is divided into four quadrants. The first major tick mark interval in each quadrant (i.e., the interval closest to the origin [0,0]) uses a linear scale, while the other intervals are logarithmic. The large filled circles show the outflow interval averages, similar to Figures 5–8, while the points are individual 1-s data points. The regression parameters are determined from the outflow averages, while the Spearman rank correlation coefficient uses the individual 1-s data.

values on a logarithmic scale, except for the major tick mark interval nearest the origin, where the scale is linear.

[32] Two correlation coefficients are shown in Figure 9. The first corresponds to the regression of the outflow averages, represented by large circles. The second is the Spearman rank correlation coefficient [*Pollard*, 1977], where the correlation coefficient is determined by the pair-wise ranking (or order) of the data. This test statistic measures the more general ordering of the data, (e.g., a high correlation would be found if large values of ion fluxes are associated with large electron densities) but makes no assumptions concerning the underlying functional relationship, other than monotonicity. The precipitating electron density is defined by (2) for both outflow averages and point by point comparisons. In the case of the outflow averages both the electron energy and number flux are downward, and n_{ep} as defined by (2) is a real number. For the 1-s data, however, the energy flux and number flux may be of opposite sign, and in that case n_{ep} is imaginary. The imaginary data cannot be included in the scatterplot or in the rank correlation. We find that for the 39,372 original 1-s averages, 10,976 (27.88%) have an imaginary number density, n_{ep}. On the basis of the analysis presented here, whereby the density of precipitating electrons is determined to be the best electron parameter for controlling ion outflows, we have also investigated the correlation between ion outflows and the electron density inside the loss cone, calculated directly from integration of the electrons spectra, rather than through the ratio of fluxes as given by (2). Similar results are obtained using the loss cone density for both the averages (correlation coefficient 0.826) and the 1-s data (Spearman rank correlation 0.384). Future investigations could therefore use the density within the loss cone as the defining parameter.

[33] As a general result for densities greater than $\sim 3 \times 10^{-2}$ cm^{-3}, the correlation provided by the outflow averages is a reasonable representation of the underlying data. For densities below this the flux appears to asymptote to a value around 10^6 cm^{-2} s^{-1}. This may be the polar wind. The fluxes are somewhat lower than those reported by

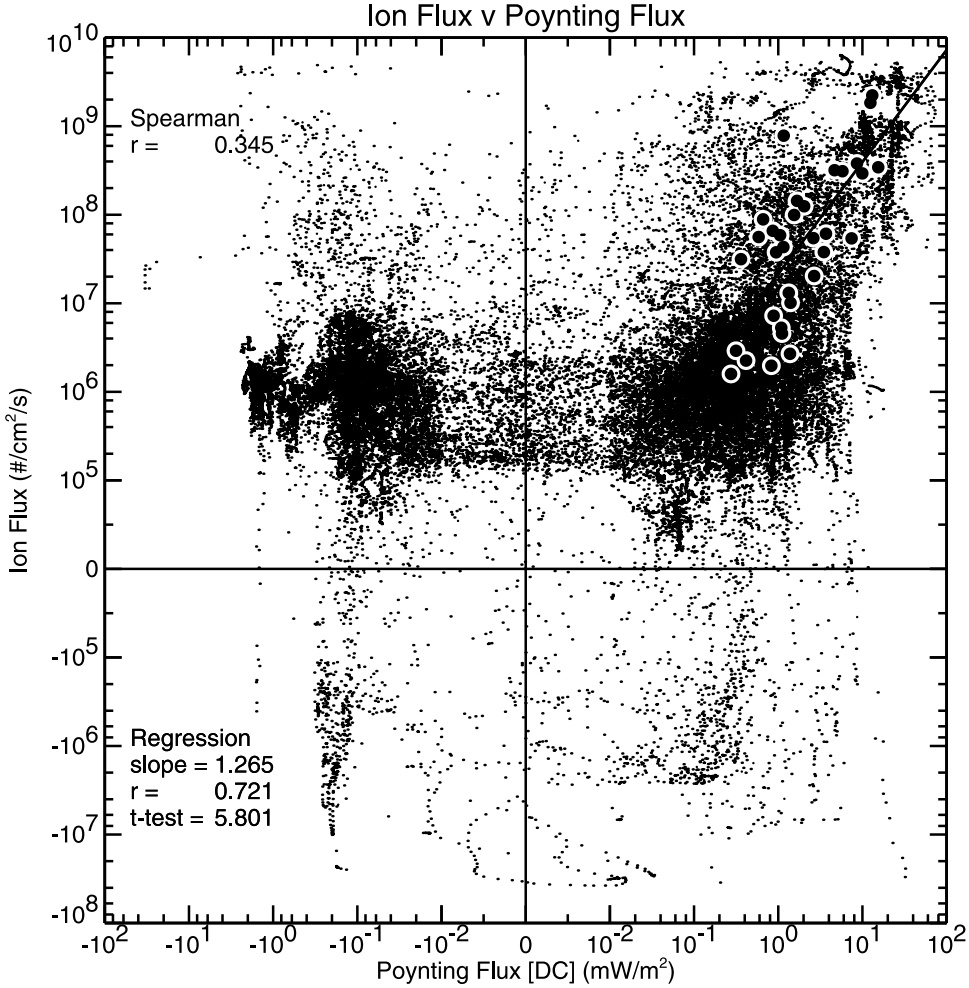

Figure 10. Scatterplot showing relationship between DC Poynting flux and ion flux, similar in format to Figure 9.

Chandler et al. [1991], but that may be a consequence of the 4 eV lower-energy cutoff used in our study.

[34] On the basis of the regression shown in Figure 9 we obtain the following scaling law for ion outflow fluxes:

$$f_i = 1.022 \times 10^{9\pm0.341} n_{ep}^{2.200\pm0.489}, \quad (3)$$

where f_i is the ion flux at 4000 km in cm^{-2} s^{-1} and n_{ep} is defined by (2), also at 4000 km. The ranges on the exponents are 95% confidence limits. We have expressed the confidence limit on the exponents because the correlation uses log-log regression. Since n_{ep} is raised to a noninteger power, (3) implicitly assumes n_{ep} is positive. The scale factor should be modified appropriately for different altitudes. Both f_i and n_{ep} scale with the magnetic field magnitude. The scale factor should therefore be reduced by about a factor of 3 if evaluated at 1000 km altitude and a factor of 4 if evaluated at 100 km altitude.

[35] The scaling law obtained using the loss cone density is

$$f_i = 9.510 \times 10^{8\pm0.373} n_{elc}^{2.240\pm0.559}, \quad (4)$$

where n_{elc} is the electron density in the loss cone. The regression parameters shown in (4) are well within the 95% confidence limits of (3). We will consequently use (3) as the electron precipitation scaling law with the electron density either given by (2) or by direct integration of electron fluxes within the loss cone.

[36] In (3) once n_{ep} is less than 4.3×10^{-2} cm^{-3} the ion flux is less than 10^6 cm^{-2} s^{-1}, which we have assumed is the asymptotic level associated with the polar wind. Thus (3) should be taken to only provide an accelerated (conic) ion outflow flux scaling law. The polar wind should be included as a separate, independent, flux.

[37] Figure 10 presents a similar analysis comparing ion outflows to the DC Poynting flux. As in Figure 9, the outflow averages are positive for both outflow fluxes and Poynting flux. On a point by point basis, however, there are a significant number (34% of the total) of Poynting flux 1-s averages that are negative. The negative Poynting fluxes are generally below 2 mW/m^2. It is possible that these represent ionospheric flows driven by the neutral wind dynamo, but it seems more probable that this is simply an effect of an offset in the magnetic field measurement that remains as a consequence of uncertainties in the determination of the background field. The model field used in this study is the 1995 IGRF field with secular variation. The model field could be improved by including models such as the

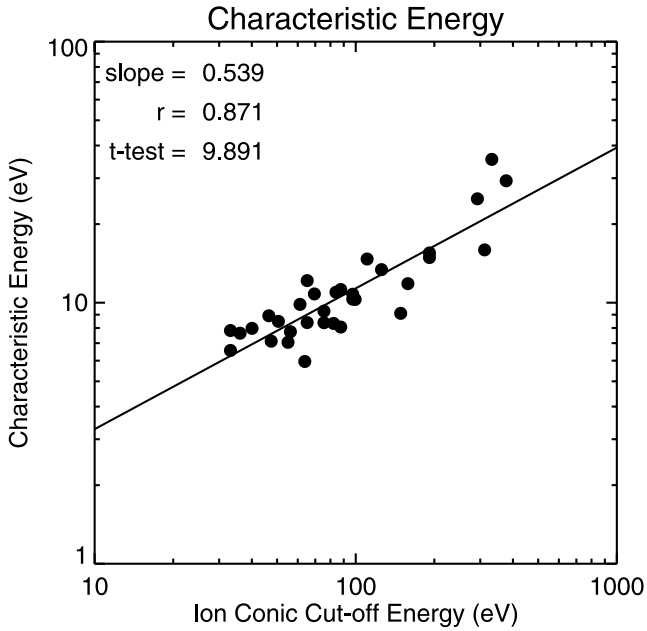

Figure 11. Characteristic ion conic energy as a function of ion conic cutoff energy. The characteristic energy is determined by the ratio of the net field-aligned energy flux to number flux.

Tsyganenko 96 model, although at polar latitudes the primary affect of this model is to introduce a vertical component related to D_{st}. In addition, the effects of field-aligned currents should be turned off in the model, as it is these currents that provide the Poynting flux into the ionosphere. It is also worth noting that the negative Poynting fluxes tend to occur at high latitudes in the polar cap, where the magnetic field perturbations are weaker.

[38] We obtain the following scaling law from the correlation shown in Figure 10:

$$f_i = 2.142 \times 10^{7\pm0.242} S^{1.265\pm0.445}, \quad (5)$$

where f_i is again the ion flux at 4000 km in cm^{-2} s^{-1}, and S is the Poynting flux at 4000 km in mW/m^2. As was the case for (3), the fluxes should be scaled with the magnetic field ratio if mapped to other altitudes. Since the exponent is near unity in (5), this is less critical than for (3). In addition, the noninteger exponent implies that S is positive. Furthermore, the ion flux drops below the nominal polar wind level of 10^6 cm^{-2} s^{-1} when S is less than 0.30 mW/m^2.

[39] If either (3) or (5) are to be used as scaling laws relating energy inputs to ion outflows, it is also necessary to specify some other characteristics of the outflows, as these will have relevance to the ultimate fate of the ions. For this particular study the ions conics are dominated by oxygen ions, as determined through visual inspection of ion composition summary plots. In addition the average characteristic energy of the conics is approximately a tenth of the cutoff energy of the conic, as shown in Figure 11. The cutoff energy was determined through visual inspection of the spectra (see, e.g., Figure 2, where the cutoff energy for the flux integration was chosen as 300 eV). Not addressed in this study is what additional acceleration occurs at higher altitudes. Nor do we address what determines the conic energy. For scaling law purposes we suggest that the conic be assumed to have a characteristic energy, given by the ratio of the energy flux to number flux, of the order 10–30 eV. The characteristic energy tends to be dominated by the perpendicular energy since $W_c \approx (2W_\perp + W_\parallel)/3$, where W_c is the characteristic energy and $W_\perp$ and $W_\parallel$ are the corresponding perpendicular and parallel energies.

5. Conclusions

[40] We have investigated the controlling parameters for ionospheric outflows as measured by the FAST spacecraft in the dayside high-latitude ionosphere, around 4000 km altitude. Figure 1 summarizes our results. The left-hand side shows the pathway controlled by Poynting flux, where the dissipation associated with ion-neutral drag results in ion heating and upwelling. The right-hand side shows the pathway controlled by electron precipitation, where electron heating and the associated ambipolar electric field also causes ion upwelling. Because the upwelling ions may not have sufficient energy to overcome gravity, especially if they are oxygen ions, additional wave heating is required so that the ions form a conic distribution that is expelled via the magnetic mirror force. At 4000 km altitude the ions are predominantly observed as conics, at least in the dayside.

[41] On the basis of the analysis of FAST data we find that the best controlling parameter is the precipitating electron density. The scaling law is given by (3), with the density either determined by (2) or by direct integration of fluxes within the loss cone. Given the strong interdependence of the different parameters, this does not mean that ion heating driven by Poynting flux is not relevant, only that the effects of Poynting flux can be subsumed within the electron density scaling law.

[42] The scaling law given by (3) applies to 4000 km and should be mapped using the magnetic field ratio if it is to be used at other altitudes. Both the density and flux are proportional to the magnetic field magnitude. Another aspect related to (3) being determined using local measurements is that we have not taken into account any processes occurring at higher altitudes. This may affect both the downgoing electron fluxes, as well as the net ion flux. Both of these effects will modify the applicability of the scaling law. In particular, additional acceleration or heating of electrons injected into the cusp from the magnetosheath may make using the scaling law particularly difficult for global magnetohydrodynamic simulations. Such simulations may, for example, be able to specify the density, temperature, and parallel streaming velocity of magnetosheath electrons as they enter the magnetosphere, but they cannot follow any additional evolution of the electron distribution along the flux tube. For this reason, the Poynting flux scaling law given by (5) may be a useful alternative. The large-scale Poynting flux is a relatively easily derived parameter for global simulations.

[43] The scaling laws given by (3) and (5) are a useful beginning for parameterizing ion outflow fluxes as a function of local input parameters. Missing from these scaling laws, however, are other factors such as ion composition, characteristic ion energy, and solar cycle and seasonal dependencies. Our initial study suggests that the ion conic

characteristic energy is of the order 10–30 eV, but more statistics would be useful in better constraining this parameter. In addition, we should determine what controls the conic energy. Also for this study the ion conics were found to be predominantly oxygen ions, but seasonal and solar cycle effects could change the composition. We also have not addressed the role of large-scale parallel electric potentials in affecting these flows, which could affect outflows in the nightside ionosphere.

[44] Because of the strong interdependence of the various parameters used in this study we have not been able to establish the relative importance of the physical processes associated with the two pathways shown in Figure 1. This appears to require a more detailed comparison between ground-based and space-based observations, with the former providing information on the state of the ionosphere at the foot of the flux tube. In particular, such observations should provide information on the occurrence of electron and ion heating within the E and F region ionosphere.

[45] In conclusion, (3) and (5) provide useful scaling laws for ion outflows related to soft electron precipitation and downward Poynting flux, with (3) being the better of the two. The choice to use (3) or (5) depends on the available input parameters. Simulations, for example, may only provide Poynting flux. The scaling laws are not additative, and even if both precipitating electron density and Poynting flux are available as input parameters, only one should be used for a particular application, although comparing and contrasting the results obtained by using the different scaling laws might be a useful exercise. Furthermore, the scaling laws should be used in conjunction with classical polar wind models. Further work to improve the applicability of the scaling laws should address the role of Alfvén waves, as well as extending the study to the nightside auroral region, to different seasons, and to different phases of the solar cycle.

Appendix A

[46] In creating the database used for the statistical study presented here, we have made decisions such as restricting the energy range over which ion and electron differential number fluxes are integrated when specifying fluxes and also the filtering used to specify the "DC" Poynting flux. The rational behind these decisions is discussed in more detail here. We also discuss the renormalization of the wave spectra acquired by FAST used to specify the ELF wave environment, as well as the correlation between wave amplitudes and Poynting flux.

A1. Energy Range Restrictions

[47] Figure 2 shows ion and electron energy and pitch angle differential energy flux spectra. Calculating number and energy fluxes requires integrating over energy and pitch angle. We have elected to integrate over all pitch angles, as we are interested in net fluxes. The energy ranges used, however, require further discussion. First, for the electrons, we have restricted the integrals to energies greater than 50 eV. This energy was chosen so that the photoelectrons would be excluded from the integrals. A band of relatively uniform background fluxes below 50 eV is apparent throughout the pass shown in Figure 2. This band is particularly clear toward the right-hand side of the figure, where a flux of $\sim 10^7$ eV/cm^2/s/sr/eV is observed in the upgoing loss cone. These are presumably atmospheric photoelectrons, and their fluxes would reduce the net downward flux if included in the integrals. It should be remembered that we are primarily interested in calculating the fluxes of precipitating electrons.

[48] With regard to the ion fluxes, we have elected to restrict both the upper and lower limits of the flux integrals. First, we use 4 eV as the lower limit. This is lower than the energy corresponding to the escape velocity for oxygen ions ($\sim$10 eV). Second, we restrict the fluxes to energies that include the conic but exclude precipitating magnetosheath ions. For example, in the case of orbit 8276 (Figure 2) ion fluxes are restricted to below 300 eV. This upper limit is chosen by visual inspection but is usually of the order 100 eV. The cutoff values used are plotted on the abscissa in Figure 11. It could be argued that we should restrict the ion energies to being above escape velocity energy, but since we do not know what additional acceleration or heating occurs at higher altitudes, the 4 eV limit provides an upper bound on the fluxes. We find that if we restrict the fluxes to energies above 10 eV then 17.7% of the 37,603 1-s average ion fluxes that were positive assuming a 4 eV lower limit are now negative. The fraction of negative fluxes increases to 40.9% if we also include fluxes above the conic cutoff energy.

A2. Frequency Filtering

[49] The electric and magnetic field measurements are acquired by FAST at a variety of data rates, depending on the instrument mode. For the purposes of the present study we wished to use data with the same data rate across all experiments. For the fields instrumentation this was achieved by a series of smoothing and decimation operations. As an example, 32 sample per second (sps) data were reduced to 8 sps data by first performing a 7-point smoothing of the higher-rate data and then using every fourth smoothed point to create the 8 sps data. This approach was applied in a successive manner to reduce the data to 1 sps (each step involved at most a factor of four reduction in data rate). The 1 sps where then further smoothed with a 7-point smoother. The smoothed data were taken to be "DC" measurements, while the difference between the smoothed data and the 1 sps data provided measurements with a nominal pass band of 0.125 to 0.5 Hz.

[50] Figure A1 shows the magnitude of the "DC" and "1 sps" electric and magnetic field data acquired on the dayside for orbits 8260–8292. The black points correspond to the "DC" measurements, while the grey points are the "1 sps" data. The two data sets cluster in different areas of the plot. The diagonal lines show the expected E to B relationship for a height-integrated Pedersen conductivity of 8 S (black line), and an Alfvén speed of 1000 km/s (grey line). While there is a large amount of scatter, it is reasonable to state that the filtering has separated the electric and magnetic field measurements into those fields associated with current closure in the ionosphere (DC) and those fields associated with Alfvénic fluctuations (1 sps).

A3. ELF Measurements

[51] The FAST instrument complement includes an onboard Fast Fourier Transform (FFT) capability, using a

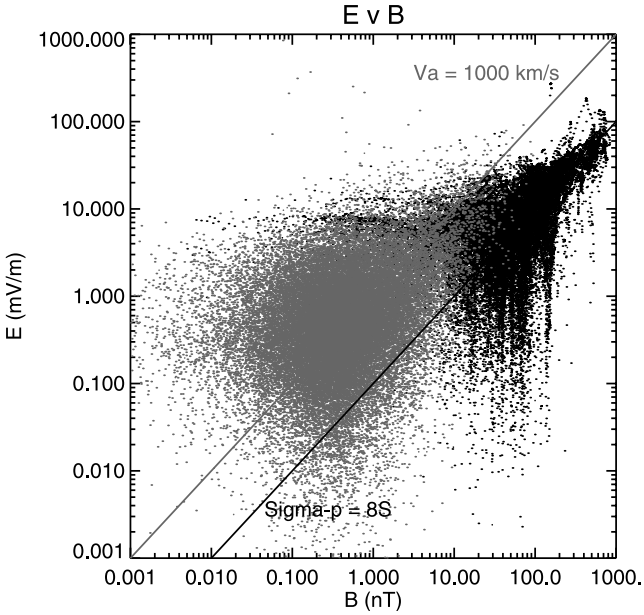

Figure A1. Comparison of electric and magnetic field measurements for "DC" signals (black points) and low-frequency [0.125–0.5 Hz] signals (grey points). The DC signals cluster near the ratio defined by a height-integrated Pedersen conductivity of 8 S. The wave-like signals seem to be better ordered by the Alfvén speed, assumed of order 1000 km/s.

Digital Signal Processor (DSP). Examples of the DSP data are shown in Figure 2e. In order to characterize the wave environment for the purposes of this study we have integrated the wave spectra over frequency to give a net ELF wave amplitude. It was found that the resultant amplitudes were much larger than expected. We attribute this to a normalization factor not included in the onboard processing. In order to determine the normalization factor we have compared the power spectra as reported by the DSP with FFTs of the 16 kHz burst mode data. Figure A2 shows a comparison for orbit 8292. The upper panel shows FFTs of the 16 kHz burst mode data. The lower panel shows the DSP data but reduced by a factor of 2000 from that reported by the DSP. Both panels use the same dynamic range, and there is reasonable agreement between the two spectra, at least above 100 Hz. Since the data are used for correlative studies with log-log regression, the normalization does not affect our conclusions. Nevertheless, we have reduced all the DSP-calculated power spectral densities by the factor of 2000 in this study.

[52] In the body of the paper we also noted that there was a strong correlation between the DSP-reported wave amplitudes and the DC Poynting flux. It is not clear if this correlation is causal, in the sense that ELF wave activity increases when the Poynting flux is large, or if the correlation is caused by "DC" electric fields contributing power to the DSP-calculated power spectra. Figure A3 shows the regression analysis for ELF amplitude as a function of DC Poynting flux. The data are plotted on a log-log scale, except for the points in the first interval between major tick marks, where the scale is linear. The large circles compare averages over the intervals of ion outflows, with the points showing individual 1-s points. The averages are clearly correlated, and the underlying data points tend to cluster about the regression line. It is also apparent that there is a lower bound to the ELF amplitudes. This lower bound varies roughly as the square root of the Poynting flux. This would be expected if the ELF spectra included some

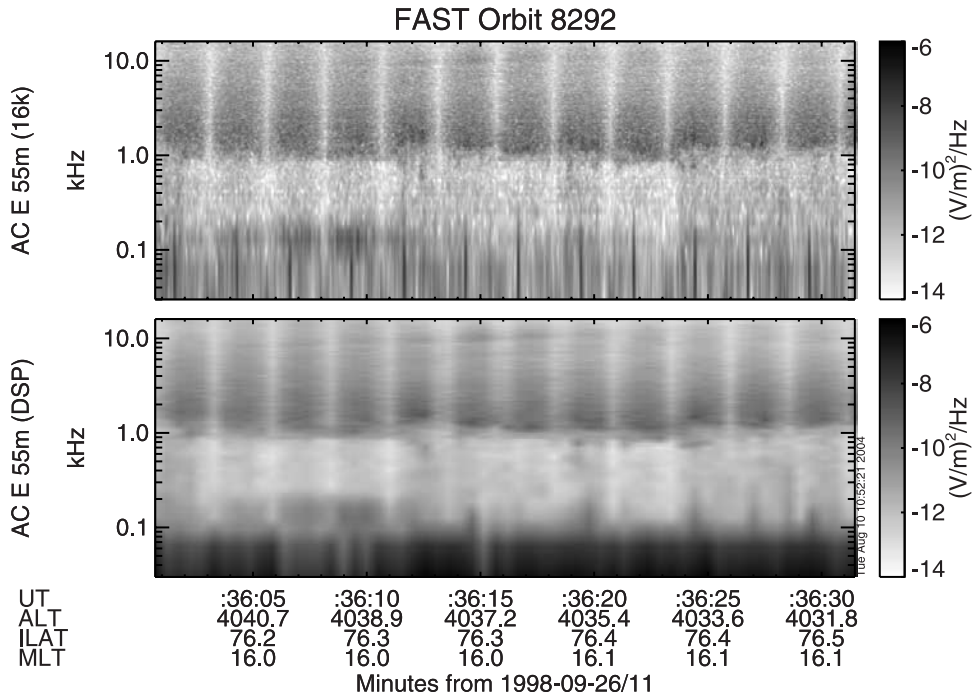

Figure A2. Comparison of wave spectra obtained by Fast Fourier Transform of 16 kHz burst-mode data (top) and the onboard Digital Signal Processor (DSP) (bottom). The DSP data have been renormalized by dividing by 2000.

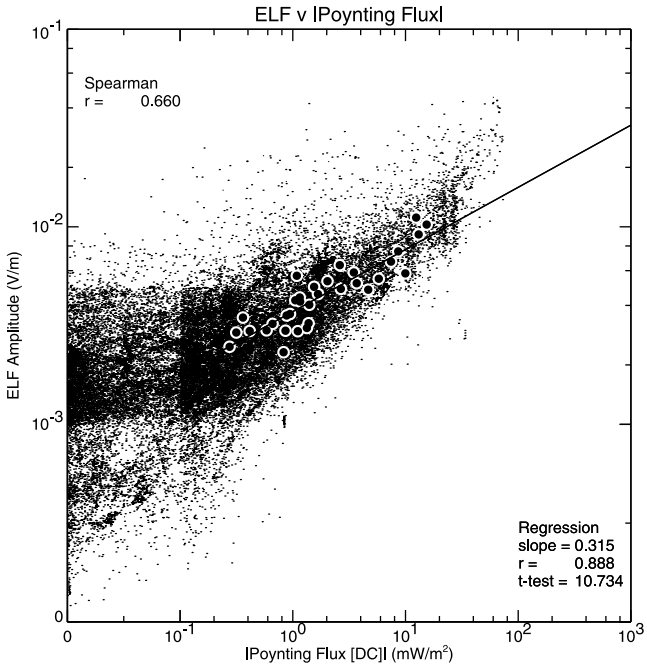

Figure A3. Scatterplot of ELF amplitude as a function of the magnitude of the DC Poynting flux.

fraction of the large-scale (DC) electric field. We conclude from Figure A3 that the ELF spectra include a mixture of both large-scale and wave electric fields. As the large-scale electric field decreases, the wave fields dominate. Thus while some of the correlation is caused by DC fields leaking in to the power spectral estimates, there is a contribution from the wave fields themselves. The present study does not explicitly address the role of wave acceleration in controlling outflows. This will be investigated further in a future paper.

[53] **Acknowledgments.** This work was supported at UCLA by NASA grant NAG5-12590 and NSF grant ATM-0208498. This is IGPP publication 6214.

[54] Arthur Richmond thanks the reviewers for their assistance in evaluating this paper.

References

André, M., P. Norqvist, L. Andersson, L. Eliasson, A. I. Eriksson, L. Blomberg, R. E. Erlandson, and J. Waldemark (1998), Ion energization mechanisms at 1700 km in the auroral region, *J. Geophys. Res.*, *103*, 4199–4222.

Banks, P. M., and G. Kockarts (1973), *Aeronomy, Part B*, Elsevier, New York.

Carlson, C. W., R. F. Pfaff, and J. G. Watzin (1998), The Fast Auroral Snapshot (FAST) mission, *Geophys. Res. Lett.*, *25*, 2013–2016.

Chandler, M. O., J. H. Waite Jr., and T. E. Moore (1991), Observations of polar ion outflows, *J. Geophys. Res.*, *96*, 1421–1428.

Cladis, J. B. (1986), Parallel acceleration and transport of ions from polar ionosphere to plasma sheet, *Geophys. Res. Lett.*, *13*, 893–896.

Cowley, S. W. H. (1981), Magnetospheric asymmetries associated with the Y-component of the IMF, *Planet. Space Sci.*, *29*, 79–96.

Crooker, N. U. (1979), Dayside merging and cusp geometry, *J. Geophys. Res.*, *84*, 951–959.

Hamrin, M., P. Norqvist, T. Hellström, M. André, and A. I. Eriksson (2002), A statistical study of ion energization at 1700 km in the auroral region, *Ann. Geophys.*, *20*, 1943–1958.

Horwitz, J. L. (1996), Multiscale processes in ionospheric plasma outflows, in *Physics of Space Plasmas (1995)*, edited by T. Chang and J. Jasperse, pp. 227–235, MIT Cent. for Theor. Geo/Cosmo Plasma Phys., Cambridge, Mass.

Liu, C., J. L. Horwitz, and P. G. Richards (1995), Effects of frictional ion heating and soft-electron precipitation on high-latitude *F*-region upflows, *Geophys. Res. Lett.*, 2713–2716.

Moore, T. E., W. K. Peterson, C. T. Russell, M. O. Chandler, M. R. Collier, H. L. Collin, P. D. Craven, R. Fitzenreiter, B. L. Giles, and C. J. Pollock (1999), Ionospheric mass ejection in response to a coronal mass ejection, *Geophys. Res. Lett.*, *26*, 2339–2342.

Ogawa, Y., R. Fujii, S. Buchert, S. Nozawa, S. Watanabe, and A. van Eyken (2000), Simultaneous EISCAT Svalbard and VHF radar observations of ion upflows at different aspect angles, *Geophys. Res. Lett.*, *27*, 81–84.

Peterson, W. K., H. L. Collin, A. W. Yau, and O. W. Lennartsson (2001), Polar/Toroidal Imaging Mass-Angle Spectrograph observations of suprathermal ion outflow during solar minimum conditions, *J. Geophys. Res.*, *106*, 6059–6066.

Pollard, J. H. (1977), *A Handbook of Numerical and Statistical Techniques*, Cambridge Univ. Press, New York.

Pollock, C. J., T. E. Moore, D. Gurnett, J. A. Slavin, and J. H. Waite Jr. (1988), Observations of electric and magnetic field signatures in association with upwelling ion events, *Eos Trans. AGU*, *69*(44), 1396.

Strangeway, R. J., and R. G. Johnson (1983), Mass composition of substorm-related energetic ion dispersion events, *J. Geophys. Res.*, *88*, 2057–2064.

Strangeway, R. J., C. T. Russell, C. W. Carlson, J. P. McFadden, R. E. Ergun, M. Temerin, D. M. Klumpar, W. K. Peterson, and T. E. Moore (2000), Cusp field-aligned currents and ion outflows, *J. Geophys. Res.*, *105*, 21,129–21,142.

Winglee, R. M., D. Chua, M. Brittnacher, G. K. Parks, and G. Lu (2002), Global impact of ionospheric outflows on the dynamics of the magnetosphere and cross-polar cap potential, *J. Geophys. Res.*, *107*(A9), 1237, doi:10.1029/2001JA000214.

Yau, A. W., and M. André (1997), Sources of ion outflow in the high latitude ionosphere, *Space Sci. Rev.*, *80*, 1–25.

Zhou, X. W., C. T. Russell, and G. Le (2000), Local time and interplanetary magnetic field B_y dependence of field-aligned currents at high altitudes, *J. Geophys. Res.*, *105*, 2533–2539.

C. W. Carlson, Space Sciences Laboratory, University of California, Berkeley, CA 94720, USA.

R. C. Elphic, Los Alamos National Laboratory, Los Alamos, NM 87545, USA.

R. E. Ergun and Y.-J. Su, Laboratory for Atmospheric and Space Physics, University of Colorado, Boulder, CO 80303, USA.

R. J. Strangeway, Institute for Geophysics and Planetary Physics, University of California, Los Angeles, CA 90095, USA. (strange@igpp.ucla.edu)